Defect and structural imperfection effects on the electronic properties of BiTeI surfaces

Defect and structural imperfection effects on the electronic properties of BiTeI surfaces

**Sebastian Fiedler[1], Lydia El-Kareh[2], Sergey V Eremeev[3,4],
Oleg E Tereshchenko[4,5,6], Christoph Seibel[1], Peter Lutz[1],
Konstantin A Kokh[4,5,7], Evgueni V Chulkov[4,8,9], Tatyana V Kuznetsova[10],
Vladimir I Grebennikov[10], Hendrik Bentmann[1,11], Matthias Bode[2] and
Friedrich Reinert[1,11]**

[1] Universität Würzburg, Experimentelle Physik VII, D-97074 Würzburg, Germany
[2] Universität Würzburg, Experimentelle Physik II, D-97074 Würzburg, Germany
[3] Institute of Strength Physics and Materials Science, 634021 Tomsk, Russia
[4] Tomsk State University, 634050 Tomsk, Russia
[5] Novosibirsk State University, 636090 Novosibirsk, Russia
[6] Institute of Semiconductor Physics, 636090 Novosibirsk, Russia
[7] Institute of Geology and Mineralogy, SB RAS, 630090 Novosibirsk, Russia
[8] Donostia International Physics Center (DIPC), E-20018 San Sebastián/Donostia, Basque Country, Spain
[9] Departamento de Física de Materiales and Centro Mixto CSIC-UPV/EHU, Facultad de Ciencias Químicas, Universidad del Pais Vasco/Euskal Herriko Unibertsitatea, Apdo. 1072, E-20080 San Sebastián/Donostia, Basque Country, Spain
[10] Institute of Metal Physics, 620041 Ekaterinburg, Russia
[11] Karlsruhe Institute of Technology KIT, Gemeinschaftslabor für Nanoanalytik, D-76021 Karlsruhe, Germany
E-mail: hendrik.bentmann@physik.uni-wuerzburg.de

Abstract

The surface electronic structure of the narrow-gap seminconductor BiTeI exhibits a large Rashba-splitting which strongly depends on the surface termination. Here we report on a detailed investigation of the surface morphology and electronic properties of cleaved BiTeI single crystals by scanning tunneling microscopy, photoelectron spectroscopy (ARPES, XPS), electron diffraction (SPA-LEED) and density functional theory calculations. Our measurements confirm a previously reported coexistence of Te- and I-terminated surface areas

originating from bulk stacking faults and find a characteristic length scale of ∼100 nm for these areas. We show that the two terminations exhibit distinct types of atomic defects in the surface and subsurface layers. For electronic states resided on the I terminations we observe an energy shift depending on the time after cleavage. This aging effect is successfully mimicked by depositon of Cs adatoms found to accumulate on top of the I terminations. As shown theoretically on a microscopic scale, this preferential adsorbing behaviour results from considerably different energetics and surface diffusion lengths at the two terminations. Our investigations provide insight into the importance of structural imperfections as well as intrinsic and extrinsic defects on the electronic properties of BiTeI surfaces and their temporal stability.

Keywords: electronic structure, spin–orbit coupling, surface morphology, semiconductor surfaces

1. Introduction

Narrow-gap semiconductors composed of heavy elements have recently attracted great interest in condensed matter research because strong spin-orbit coupling leads to unexpected effects in their electronic structure. Prominent examples are topological insulators such as Bi_2Se_3 or Bi_2Te_3 that feature non-trivial spin-polarized surface states as a result of a spin–orbit driven inversion of the bulk band gap [1–3]. Another appealing class of semiconductors are the bismuth tellurohalides BiTeX (X = I, Br, Cl) whose non-centrosymmetric crystal structure allows for giant Rashba-type spin-orbit splittings of bulk and surface electronic bands as was demonstrated previously by angle-resolved photoemission (ARPES) experiments [4–11] and density functional theory (DFT) calculations [12–16]. Optical transition [17], magneto-optical [18, 19] and transport measurements [20–22] are in accordance with a spin splitting of the valence and conduction band. For BiTeX it may also be possible to induce a topological phase transition by application of hydrostatic pressure [23–27].

In order to utilize topological insulators or giant-Rashba semiconductors in functional devices or to probe their spin-dependent transport properties, a stable and well-defined electronic structure is required. However, the surface electronic structures of the above mentioned materials show a strong sensitivity towards changes of the structural and chemical surface properties, including surface morphology and termination [6, 28, 29], intrinsic defects [30], or the presence of adsorbates [31–34]. In the particular case of BiTeI previous works showed that the (0001) surface, which is usually obtained by the cleavage of single crystals, can be inhomogeneous and can exhibit two different domain types with individual electronic band structures [6, 7, 35]. BiTeI has a hexagonal non-centrosymmetric crystal structure built of alternating Bi, Te and I layers (figure 1(d)). The natural cleavage plane of the crystal lies between adjacent Te and I layers that show the weakest interlayer-bonding along the stacking sequence. Hence, bulk stacking faults that inverse the order of the stacking sequence can lead to two coexisting domains of different surface termination after cleavage [6, 7, 35] (see figure 1(d)). These previous observations call for additional detailed investigations of the structural and electronic properties of BiTeI surfaces.

In this work we study a complex interplay of crystal structure, surface termination, extrinsic and intrinsic defects as well as electronic structure for BiTeI(0001). The results are based on experiments on cleaved single crystals by several complementary surface science methods as well as on *ab initio* DFT and model calculations. In accordance with previous findings [7] the investigated BiTeI(0001) surfaces consist of I- and Te-terminated domains. These domains have lateral extensions of ∼100 nm and develop individual electronic band structures. The boundaries between these domains are not affected by the presence of step edges, which confirms stacking faults in the bulk crystal to be the origin for the simultaneous appearance of different terminations. An analysis of the atomic structure reveals that the two terminations feature different characteristic defect types in the surface and subsurface layers. We show that the electronic structure of BiTeI(0001) is prone to time-dependent modifications, even under ultra-high vaccuum conditions, causing energy shifts in the band structure on the order of several 100 meV. Similar effects are also observed after room temperature deposition of Cs adatoms leading to the conclusion that adsorption of residual gas atoms gives rise to the time-dependence of the surface electronic structure. Interestingly, the adatoms accumulate on I-terminated surface areas and therefore do not affect electronic states of the Te-terminated domains. We reconcile this peculiar preferential adsorption behaviour by a calculation of adsorption energies and diffusion lengths that turn out to differ considerably for the two terminations.

2. Methods

2.1. Experimental setup

The used experimental setup is designed for a comprehensive analysis of the geometric and electronic properties of solid surfaces, both in real space and in reciprocal space. It allows one to perform scanning tunneling microscopy (STM)/STS, ARPES, x-ray photoelectron spectroscopy (XPS), and spot-profile analysis low-energy electron diffraction (SPA-LEED) under ultra-high vaccuum conditions for the same sample without exposing it to air. The combined chamber setup is equipped with an Omicron variable-temperature STM (VT-STM), a Scienta R3000 electron analyzer and an Omicron SPA-LEED system. Additional, high-resolution STM experiments were performed at a separate experimental setup using an Omicron low-temperature STM (LT-STM) operated at $T = 5$ K.

BiTeI single crystals were cleaved at room temperature along the (0001) direction with a rod glued on top of the samples at pressures below $p = 2 \times 10^{-10}$ mbar. Submonolayer amounts of Cs were deposited in the VT-STM using commercial alkali dispensers (SAES Getters). All experiments were performed at room temperature except for those carried out at the LT-STM.

STM tips were electrochemically etched from a polycrystalline tungsten wire, prepared on a noble metal (111) surface before scanning BiTeI(0001). For both microscopes dI/dU maps have been taken by means of the lock-in technique with $\nu = 789$ Hz. The acquisition of dI/dU maps with variable voltage is a valuable method for surfaces with inhomogeneous terminations as it allows one to compare the density of states (DOS) on different terminations as a function of energy. Additionally, it enables a fast data acquisition which is quite important for samples exhibiting aging processes. In order to obtain such maps we started at $U = -0.05$ V decreasing the voltage gradually each 26 scan lines by 0.05 V to $U = -1$ V. All STM scans have a

resolution of 512×512 pixels resulting in 20 slices with 26×512 pixels for each voltage. The STM data were processed with the software WSxM [36].

The ARPES data were acquired with a non-monochromatized He discharge lamp with He Iα excitation (21.22 eV). The energy resolution was approximately 25 meV. XPS measurements were done with Al K$_{\alpha}$ excitation (1486.6 eV).

2.2. Crystal growth

Both synthesis and growth of BiTeI were performed in the same evacuated quartz ampoule. Since elementary iodine is very volatile, it is more convenient to prepare BiI$_3$ first. For this reason, Bi and I in the ratio $\sim 1 : 5$ were fused at 350 °C. The excess of iodine was taken in order to compensate its loss during evacuation. On the other hand, the residue of iodine may be easily distillated to the cold end of the ampoule. According to the published data, BiTeI melts congruently at 560 °C [37]. Therefore Bi, Te and BiI$_3$ taken in proportion $2 : 3 : 1$ were heated to a temperature 20 °C higher than the melting point. Crystal growth was done by a modified Bridgman method with rotating heat field [38]. After pulling the ampoules through the vertical temperature gradient ~ 15 °C cm^{-1} with a rate of 10 cm day^{-1} the furnace was switched off.

2.3. DFT

The calculations were performed within the density functional formalism as implemented in the VASP code [39, 40]. We used the all-electron projector augmented wave [41, 42] basis sets with the generalized gradient approximation of Perdew, Burke and Ernzerhof [43] to the exchange correlation potential. Relativistic effects, including spin-orbit coupling, were fully taken into account. When modeling the Cs diffusion on the BiTeI surfaces, the spin–orbit interaction was neglected. Experimental lattice parameters [45] of BiTeI were used in the calculations. The surface of BiTeI has been reported to suffer from stacking faults leading to mixed surface terminations [7]. To simulate the surface with both terminations, we used a slab composed of 24 atomic layers (which comprises Te- and I-terminated surfaces on its opposite sides) separated by roughly 20 Å vacuum space. Electronic band structure of the single Te-terminated surface was calculated using the slab with I-terminated side passivated by a hydrogen monolayer. The atomic positions for the first two surface layers of the free surfaces of the slab as well as position for passivating hydrogen layer and for Cs adatom at different adsorption sites were optimized.

## 3. Results

3.1. Surface and defect morphology

Figure 1(a) shows a large scale STM image for the BiTeI(0001) surface revealing flat terraces extending over several hundred nm in width and over several μm in length. On the individual terraces one can discern an additional mottled texture resulting from two types of surface areas that are about 10–100 nm wide and differ in contrast. A more detailed inspection of this texture is shown in the STM image in figure 1(b) that was acquired with varying gap voltage between −0.05 V and −1 V with an increment of 0.05 V. Starting at the upper part of the image a clear contrast between the two types of areas is observed which, however, fades with lowering the
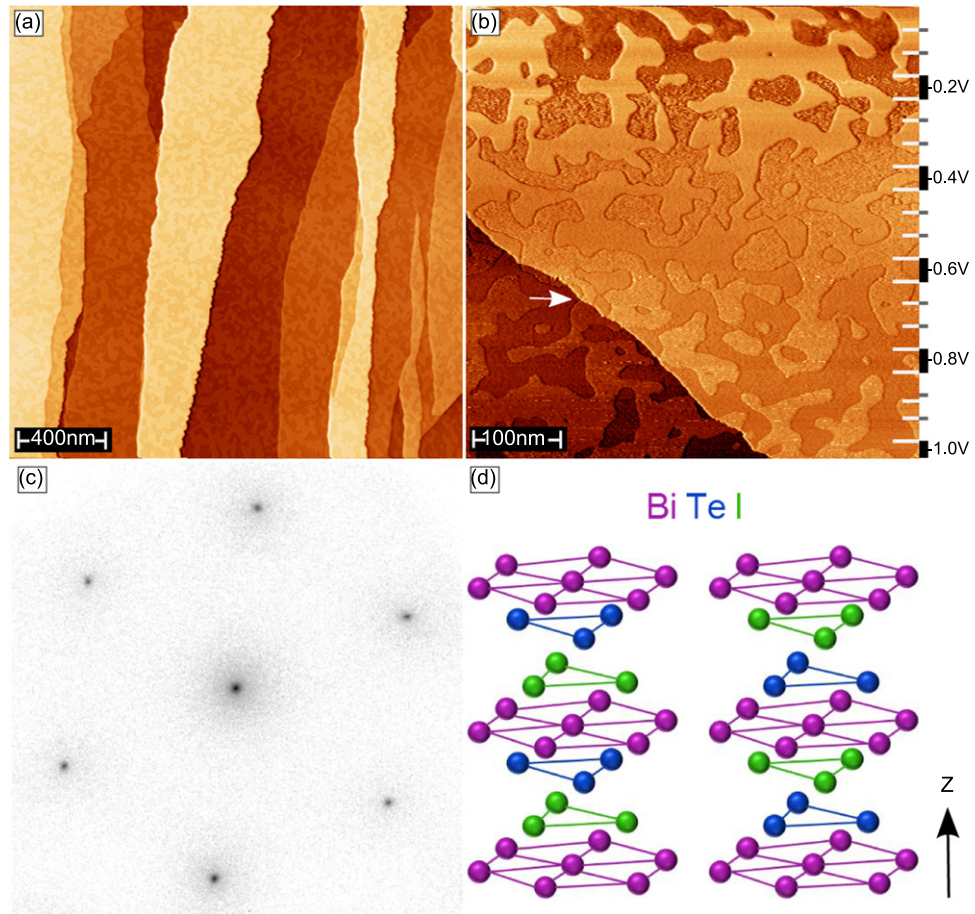
Figure 1. (a) Topography of BiTeI(0001) with $2\,\mu$m $\times$ $2\,\mu$m scan size (VT-STM, $U = -0.4$ V, $I = 0.1$ nA). In addition to flat terraces the measurement reveals a peculiar mottled texture on a smaller length scale than the step edge separation. (b) Topographic image with variable gap voltage covering an area of $500\,$nm $\times 500\,$nm (VT-STM, $I = 0.5$ nA). The mottled pattern consists of two different surface types extending over step edges (arrow) with a varying z-contrast depending on gap voltage. (c) SPA-LEED image for BiTeI(0001) acquired at room temperature and a beam energy of 93 eV. (d) Non-centrosymmetric bulk unit cell of BiTeI. Two possible layer stacking orders along the z-axis are shown which result from a rotation of the unit cell by 180°.

gap voltage, disappears at around −0.5 V, and finally inverts. This observation indicates that the two surface areas correspond to two chemically different terminations [44]. We will show later that one type of surface area is terminated by an I layer and the other one is terminated by a Te layer. Therefore, we will from now on use the terms I termination and Te termination to distinguish between the two different types of surface areas. It is important to note that both surface areas cover step edges without any apparent influence of the latter (see for example the position marked with an arrow in figure 1(b)). This indicates that the observed domains are already present in the bulk crystal and originate from stacking faults with the layer ordering being rotated by 180° (figure 1(d)). The independence of domain boundaries and step edges also allows us to determine the step height between adjacent terraces to 7 Å on both terminations which is in agreement with XRD measurements of the bulk lattice constant
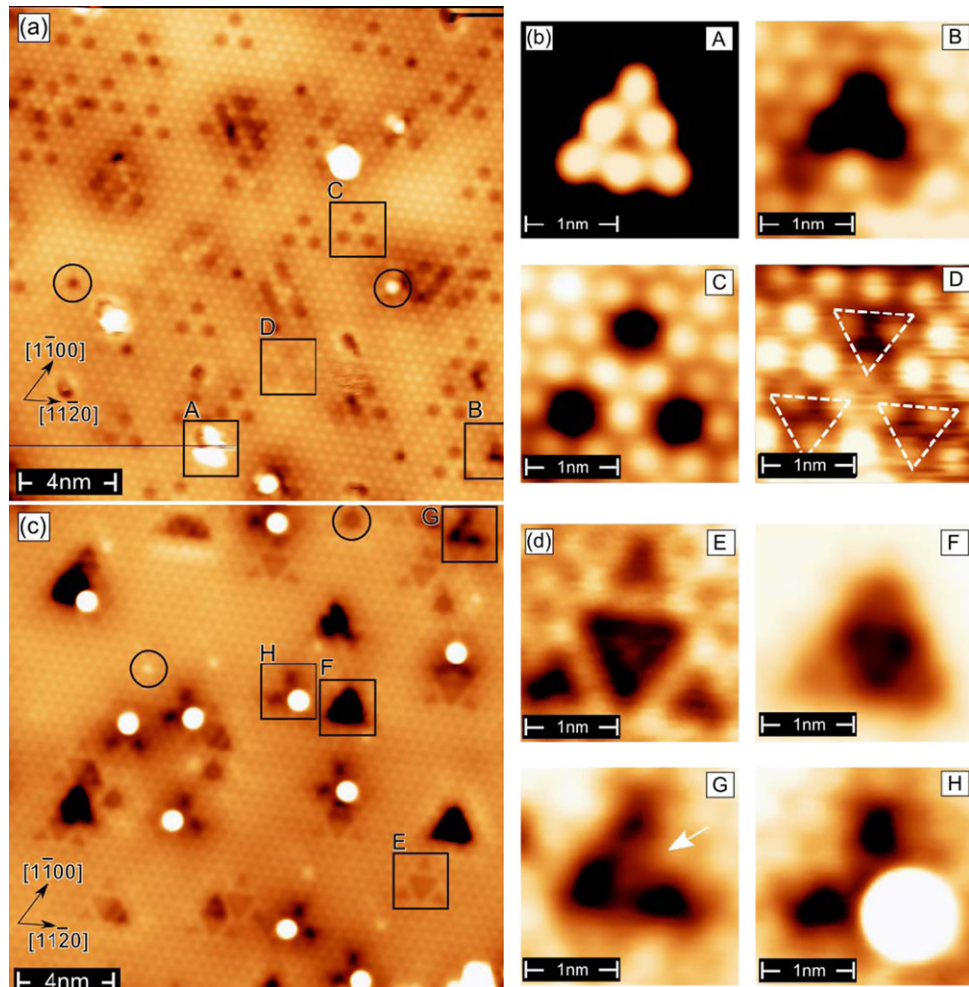
Figure 2. (a) Atomically resolved scan of the I-terminated surface part of BiTeI(0001) taken at $T = 5$ K (LT-STM, $U = -1.1$ V, $I = 0.2$ nA). Four different types of defects are identified and labeled by A, B, C, and D. (b) Close-up images of the defects on the I termination. (c) Atomically resolved scan of the Te-terminated surface part taken at $T = 5$ K (LT-STM, $U = 1.1$ V, $I = 0.2$ nA). Also on the Te termination four types of defects are observed and labeled by E, F, G and H. (d) Close-up images of the defects on the Te termination. Additional defects in the first layer of both terminations are highlighted by black circles in (a) and (c), where a dark (bright) appearance corresponds to either an antisite or a vacancy (either an antisite or an adatom in on-top position). Images sizes are 20 nm × 20 nm for (a) and (c) and 2.2 nm × 2.2 nm for all panels A–H in (b) and (d).

[45, 46]. The diffraction image in figure 1(c) represents a superposition of the signals from both terminations because the electron beam spot by far exceeds the length scale on which the two surface terminations vary. The single (1 × 1) pattern which we observe thus excludes any significant mismatch in lateral orientation or the occurrence of a reconstruction on one of the terminations. Based on figure 1(c) we determine the in-plane lattice constant to 4.3 Å, again in good agreement with previous XRD results [45, 46].

In the following we discuss the two different terminations of BiTeI(0001) surface on the atomic scale. Figures 2(a) and (c) show LT-STM images taken on an I-terminated and a Te-terminated surface area, respectively. In agreement with our SPA-LEED experiments both terminations are found to have the same crystallographic orientation. Defects within the surface layer are marked with circles in figures 2(a) and (c). Those defects with dark appearance correspond to vacancies or antisites, whereas those with bright appearance correspond to antisites or adatoms in on-top position. In addition to these surface defects, both terminations exhibit several on-surface and subsurface defects which are marked by black squares, labeled A–D (figure 2(a)) and E–H (figure 2(b)), and presented at higher magnification in figures 2(b) and (d), respectively. The total densities of defects visible in these topographic images (scanned surface area $400 \, \text{nm}^2$ each) amount to approximately 50 and 30 for the I- and Te-teminated surface, respectively. Panel (A) in figure 2(b) shows a triangular cluster that consists of six adatoms. It is centred in hollow positions of the surface I layer. These clusters are roughly 3 Å in height and often interact with the STM tip during the scanning process even at 5 K. For example, the horizontal line in the bottom part of figure 2(a) indicates such a material transport during the scan. The atomic species forming these clusters is presently unknown, but the most plausible origin are Te atoms that remain on the surface after the cleaving and arrange in small clusters.

For the characterization of the remaining seven subsurface defects we follow the procedure developed by Jiang *et al* in [30]. Based on the fact that the inter-layer coupling within individual quintuple layers (in our case triple layers) originates from p-orbitals which form chains of σ bonds along [111] directions, they developed a simple and intuitively understandable interpretation scheme. The crucial assumption is that those atoms which are connected with the defect by a straight sequence of the $pp\sigma$ bonds are most strongly affected. Due to the threefold symmetric crystal structure, the surface corrugation resulting from subsurface defects must also exhibit a threefold symmetry. Because of the above-mentioned straight $pp\sigma$ bond, however, the lateral size of the defect structure grows linearly as the depth of the defect site increases. We start with the simplest defect of the I-terminated surface which is shown in panel (B) of figure 2(b). It appears as a roughly triangular depression (dark) which covers three iodine sites. According to the model of Jiang *et al* [30] the defect must be located in the second layer (Bi) which affects the three neighbouring surface atoms. This defect occurs only rarely indicating a low defect density in the Bi layer. Panel (C) also shows a triangular feature but in this case the depressions are separated by three iodine surface atoms which maintain their original corrugation. Hereafter, features with similar lateral dimensions will be called (3×3). According to its larger lateral size we attributed this feature to a defect in the third layer (Te), possibly a vacancy. Panel (D) presents another defect which is characterized by three triangular clusters of iodine atoms (triangles in panel D) with an reduced apparent height. Because of its (3×3) size we conclude that this defect is also located in the third layer (Te) and possibly originates from a Bi or I antisite. For the Te-terminated surface we only found surface features with a (3×3) size, indicating that these subsurface defects are unanimously located in the third layer (I). The defects in panel (E) and (F) exhibit a regular threefold symmetry and are probably caused by antisites or a vacancy. Interestingly, the defects in panels (G) and (H) are asymmetric (marked by an arrow) and thus do not obey the threefold symmetry of the lattice. One possible origin for this could be a vacancy in the second layer (Bi) which was filled by an atom of the third layer (I) leaving behind a vacancy on this position. In this scenario the combination of
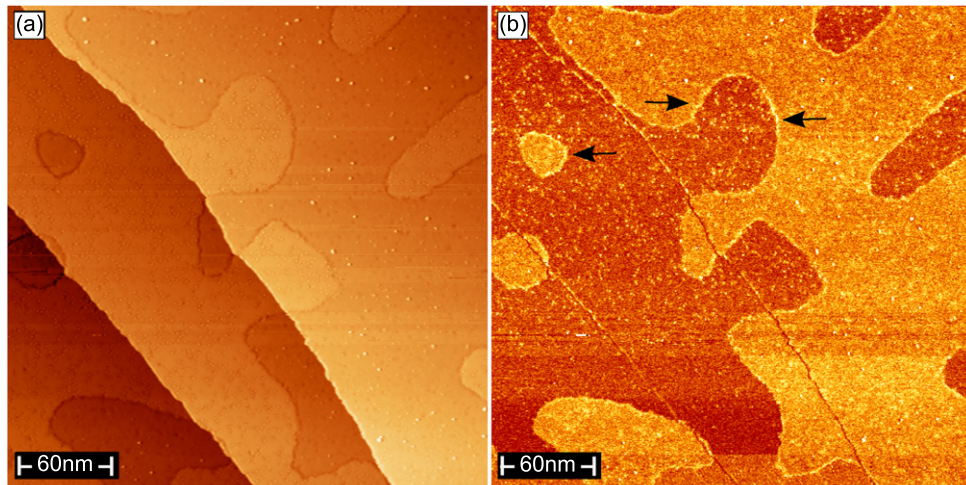
Figure 3. (a) Topography of BiTeI(0001) and simultaneously recorded dI/dU map in (b) taken at $T = 5$ K with 300 nm × 300 nm scan size (LT-STM, $U = -1$ V, $I = 0.02$ nA). The distributions of clusters (figure 2(b)(A)) on the I termination and of adsorbates (figure 2(d)(F)) on the Te termination are visible. Arrows in (b) indicate an increased density of states at the domain boundaries between both terminations.

second and third layer features breaks threefold symmetry. Indeed, close inspection reveals that defect in panel (H) corresponds to a defect as shown in panel (G) with an adsorbate at the open end. We speculate that the high electronegative charge of iodine in the second layer leads to the pinning of adsorbates and adatoms resulting from the fracturing process. Interestingly, no defects below the first triple layer were observed.

The clusters on the I termination and the bright adsorbates on the Te termination are also visible in the topographic image in figure 3(a) taken at low temperature. The dI/dU map in figure 3(b), acquired at a constant voltage of -1 V, reveals a higher DOS on the I termination at this binding energy. At the domain boundaries between two terminations we find an increased DOS (indicated by arrows). This observation points to an edge effect on the electronic charge distribution.

3.2. Surface electronic structure and adsorption properties

Due to potential changes in the near-surface layers of BiTeI(0001) and related compounds strongly spin–orbit coupled surface states split off from the bulk valence and conduction band edges [6, 7, 9, 12, 13, 15]. The potential change ΔV is negative for the Te-terminated surface and positive for the I-terminated surface. Figure 4 shows the calculated electronic structure of BiTeI(0001) slab. The simulated slab is terminated by Te layer on one side and by I layer on the opposite side. Hence, the calculated band structure in figure 4(a) can be regarded as a superposition of the surface electronic structures corresponding to the two different terminations. Bands denoted by red (blue) markers correspond to electronic states that are predominantly localized near the I-terminated (Te-terminated) surface. The two most prominent Rashba-split features are an electron-like surface band on the Te termination with a band minimum at -0.2 eV and a hole-like surface band on the I termination with a band maximum at 0.15 eV. In general, we find that the negative ΔV at the Te-terminated side of the slab leads to a
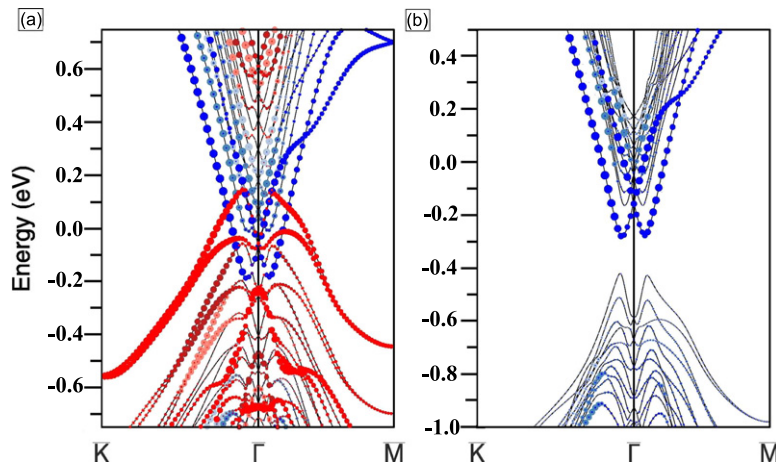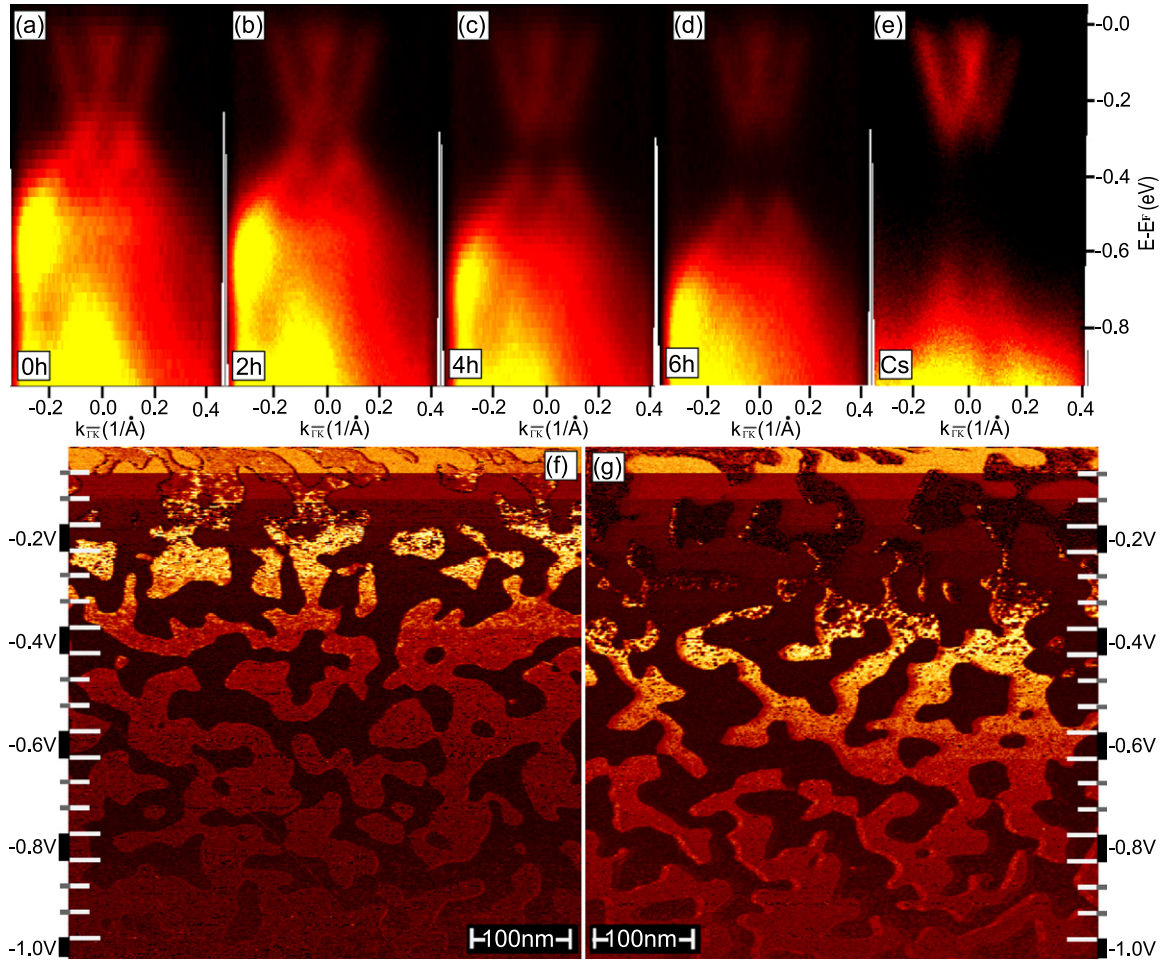
Figure 4. Surface electronic structure of BiTeI(0001) as determined by DFT. Panel (a) shows the result for a BiTeI(0001) slab that incorporates an I-terminated surface at one side of the slab and a Te-terminated surface at the opposite side. The electronic structure of the Te-terminated surface is shown in (b). In (a) and (b) states denoted by red (blue), darkred (steelblue), and pink (grey) circles are localized predominantly in the first, second and third triple layer of the I-terminated (Te-terminated) side of the slab.

downward shift of energies of the electronic states trapped in then near-surface potential while the positive ΔV at the I-terminated side of the slab produces an upward shift. As a net result, the surface states arising in the system with mixed termination overlap the gap.

Figure 5(a) shows an ARPES data set acquired for a freshly cleaved BiTeI(0001) surface. There appear an electron-like Rashba-split state at ~-0.2 meV at $\bar{\Gamma}$ and a hole-like state at lower energy. The respective band minima and maxima of the two states touch each other or even slightly overlap at wave vectors of $\pm0.1\,\mathring{A}^{-1}$. By comparison to our DFT calculations and to previous results [6, 7, 12] we identify the electron-like and the hole-like state as surface states of the Te- and I-terminated domains, respectively.

Monitoring the surface electronic structure as a function of time after cleavage we find that significant modifications of the observed spectral features take place on the time scale of hours. This time-dependence is clearly visible in the data sets in figures 5(b)–(d). While the electron-like state on the Te termination remains largely unmodified the hole-like state on the I termination gradually shifts to lower energies. After six hours we find a total energy shift of ~200 meV. The observed time-evolution of the surface electronic structure of BiTeI(0001) has not been reported previously whereas a similar 'aging' effect was found for the topological insulator surface Bi_2Se_3(0001) and attributed to band bending as a result of residual gas adsorption [32]. In order to further investigate the aging effect we intentionally deposited Cs atoms on the surface thereby mimicking the effect of residual gas atoms. An ARPES data set collected after deposition is shown in figure 5(e). The change of the spectral features is indeed similar to the one due to surface aging: while the electron-like band on the Te termination is insensitive to the adsorption, the hole-like state resided on the I termination shifts to lower energies and eventually merges with the bulk valence band. This result is in perfect agreement with calculated spectrum for the single Te termination (figure 4(b)) where only the electron-like Rashba-split states reside on the surface [12, 13]. It is also interesting to note that the

Figure 5. Electronic structure of BiTeI(0001) along $\overline{\Gamma K}$ as determined by ARPES at room temperature directly after cleavage (a) and after two (b), four (c) and six (d) hours as well as after deposition of Cs adatoms (e). Both, surface aging and Cs deposition cause a binding energy shift of the hole-like surface state on the I-terminated surface part. Panels (f) and (g) show dI/dU maps taken at room temperature with variable gap voltage (VT-STM, $I = 0.5$ nA) for clean BiTeI(0001) and after Cs deposition, respectively. The strong increase in signal on the I termination at -0.15 V in (f) corresponds to the band onset of the hole-like surface state. As inferred from panel (g) this onset is shifted to higher binding energies after Cs adsorption. The scan size of (f) and (g) is 500 nm × 500 nm.

photoemission signal of the hole-like state is more blurry than for the electron-like state. This could be due to the higher defect concentration on the I termination as compared to Te termination found in the STM measurements and due to the preferred adsorption of residual gas species. However, also energy shifts of the spectral features during the finite data aquisition time will cause an additional broadening.

To examine the selective effect of Cs adsorption directly in real space we have performed STM measurements. Figure 5(f) shows a dI/dU map taken at variable gap voltage for a clean sample before Cs deposition. The dependence of the dI/dU signal on energy clearly differs for the two terminations. On the I-terminated surface areas we find a strong increase of the signal at

around -0.15 V. The relative contrast in comparison to the Te-terminated areas becomes maximal between -0.25 V and -0.30 V. We attribute this finding to the onset of the hole-like surface state observed in the ARPES data. With further decreasing the gap voltage the contrast fades and finally almost vanishes at -1 V. Figure 5(g) shows a dI/dU map that was obtained after deposition of Cs. The most prominent difference to the map for the clean surface is an energy shift of ~200 meV for the signal measured on the I termination. The sharp rise in contrast now appears at around -0.35 V implying a lower energy position for the onset of the hole-like surface state. Note also that between -0.05 V and roughly -0.25 V the dI/dU signal is lower on the I termination which most likely results from the presence of the electron-like surface state on the Te termination.

A natural explanation for the modification of states on the I termination is the high chemical reactivity of I which may lead to a preferential positioning of adsorbates on I-terminated domains [35]. Support for this interpretation is provided by the STM measurements for Cs/BiTeI(0001) presented in figure 6(a)–(b). The topographic image in panel (a) reveals that the deposited Cs grows in islands which appear as bright spots (marked by circles). The Cs islands are one monolayer in height and have diameters of several nm. The islands are exclusively located on one termination type. Furthermore, the simultaneously recorded dI/dU map in figure 6(b) provides evidence that the Cs islands are located on the I termination which is identified by the characteristic energy dependence of its dI/dU signal discussed above. Given the large number of defects identified in the STM data in figure 2 we speculate that surface defects may act as nucleation centres and thereby promote the Cs island formation.

In order to obtain additional experimental information about the selective Cs adsorption we collected XPS data of the Te $3d_{5/2}$, I $3d_{5/2}$ and Cs $3d_{5/2}$ core levels (see figure 6(c)). The three respective spectra correspond to measurements of the clean surface in normal emission (black lines), after deposition of Cs in normal emission (red lines) and after deposition of Cs with an emission angle of 60° (blue lines). In the latter case the measurement is more surface sensitive. We find that Cs adsorption leads to a significant damping of the I $3d_{5/2}$ signal whereas the Te $3d_{5/2}$ signal remains largely unchanged. This observation is not compatible with a homogeneous distribution of Cs atoms for which similar dampings of both signals would be expected. It is in line, however, with a preferential positioning of Cs on the I-terminated surface areas. With increasing surface sensitivity the damping of the I signal is further enhanced while the Cs $3d_{5/2}$ signal is increased. This observation is indicative of the adsorbed Cs being located above the topmost substrate layers, in agreement with the STM measurements in figures 6(a)–(b).

3.3. Simulation of Cs diffusion

In order to explain the preferential positioning of Cs on I-terminated domains we have theoretically studied adsorption and diffusion of Cs adatoms on Te- and I-terminated surfaces. Our total energy calculations performed within a 4×4 surface cell with a single Cs adatom show that for both surface terminations the preferable position for a Cs adatom is the *fcc* hollow site, while the energy for the *hcp* site is only slightly higher (by 17 meV and 16 meV on Te- and I-terminated surfaces, respectively). The adsorption energy has been calculated as the difference between the total energies of Cs/BiTeI and clean BiTeI plus an isolated Cs atom. The calculations yield adsorption energies of 1.283 eV and 0.966 eV for *fcc*-adsorbed Cs on the I and the Te termination, respectively. The difference between the adsorption energies is related
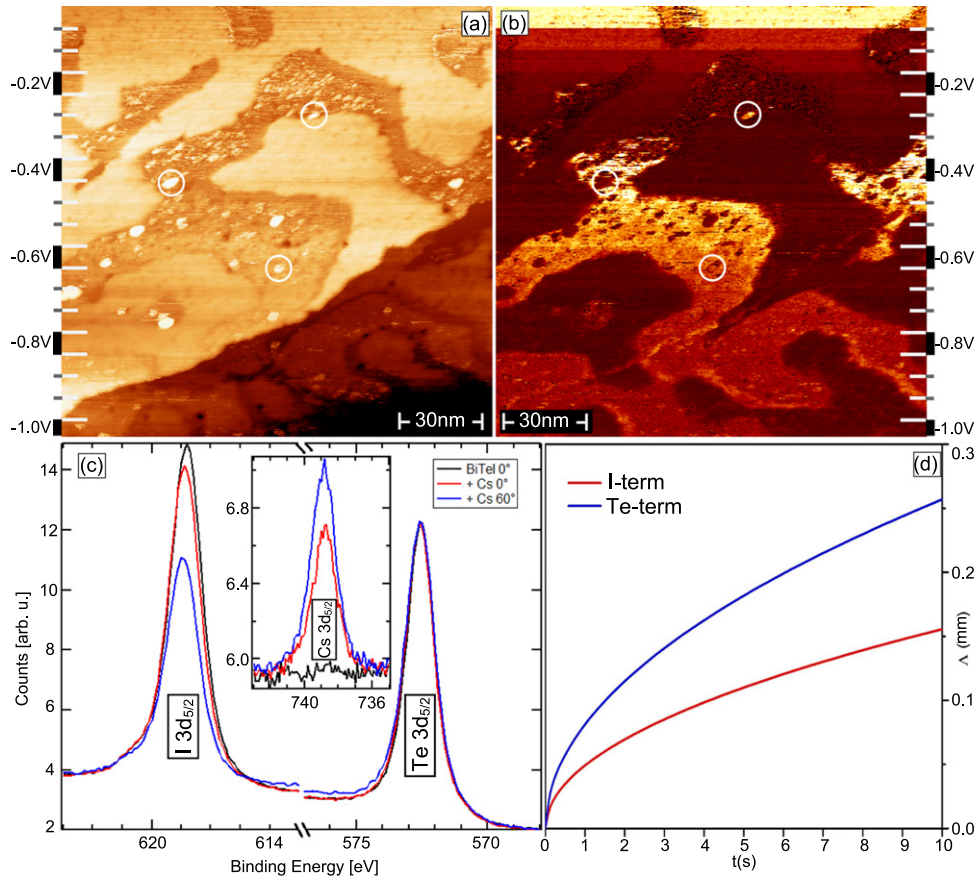
Figure 6. (a) Topographic image for Cs/BiTeI(0001) and simultaneously recorded d*I*/d*U* map in (b) taken at room temperature with variable gap voltage and 150 nm × 150 nm scan size (VT-STM, *I* = 0.5 nA). In (a) Cs islands appear as bright spots (marked by circles) on I-terminated surface areas. (c) XPS spectra of the Te $3d_{5/2}$, I $3d_{5/2}$ and Cs $3d_{5/2}$ core levels obtained for Cs/BiTeI(0001) using Al Kα excitation at room temperature. The black spectra correspond to a measurement of the clean surface before Cs deposition. The red and blue spectra were acquired after deposition with the sample oriented in normal emission and for an emission angle of 60°, respectively. (d) Calculated diffusion length Λ for room temperature Cs diffusion on Te- and I-terminated surfaces areas.

to a difference in charge transfer. On the I termination the Cs adatom donates $\sim$0.81 electrons to the substrate while for the Te termination it is only $\sim$0.76 electrons. A Cs adatom will gain an energy of 317 meV when changing its position from the Te to the I termination. This indicates that the adatoms should have a tendency to diffuse from Te-terminated to I-terminated surface areas. As deduced from our STM measurements the mean size of Te(I)-terminated surface areas is on the order of a few tens of nm. In order to diffuse from Te- to I-terminated domains on a short time scale the diffusion length for Cs adatoms on the Te termination must be larger than the size of the domains.

To estimate the diffusion mobility of Cs adatoms on Te- and I-terminated surfaces we use an approach proposed in [47]. The mean diffusion length in the low adatom coverage limit is

$$\Lambda = \sqrt{2\alpha D t}, \tag{1}$$

where α is the dimensionality of the problem (here $\alpha = 2$ for surface diffusion), t is the time and D is the tracer diffusion coefficient. According to [47] the diffusion coefficient for a 2D hexagonal lattice is defined as

$$D = \frac{6}{2\alpha} \frac{\nu_{hf} \times \nu_{fh}}{\nu_{hf} + \nu_{fh}} l^2. \tag{2}$$

Here ν_{hf} and ν_{fh} are hop rates for jumps from *hcp*- to *fcc*-sites and from *fcc*- to *hcp*-sites, respectively; l is the distance between *hcp* and *fcc* hollow sites. The hop rates are defined as

$$\nu = \frac{1}{2d} \sqrt{E_a/(2\,m)} \times e^{-E_a/(k_B T)}, \tag{3}$$

where d is the jump length which is equal to the half-distance between *fcc* and *hcp* sites, i.e. $d = l/2$; m is the mass of adatom (Cs); T is the temperature; and E_a is the activation energy for the jump. Thus, the hop rates and consequently, diffusion coefficients for Cs diffusion on Te- and I-terminated surfaces can be completely determined from the activation barriers E_a for $fcc \rightarrow hcp$ and $hcp \rightarrow fcc$ jumps.

According to our total-energy calculations the energy barriers for Cs diffusion on the I termination are 0.113 and 0.096 eV for $fcc \rightarrow hcp$ and $hcp \rightarrow fcc$ jumps, respectively, while they are slightly lower on the Te-terminated surface: 0.083 eV for $fcc \rightarrow hcp$ jumps and 0.067 eV for $hcp \rightarrow fcc$ jumps. The lower barriers on the Te termination is related to a weaker Cs/substrate bonding compared to the I termination.

The calculated room temperature (300 K) diffusion coefficients $D_{\mathrm{Te}} = 1.651 \times 10^{-5}$ and $D_{\mathrm{I}} = 0.605 \times 10^{-5}\,\mathrm{cm}^2\,\mathrm{s}^{-1}$ allow us to estimate the diffusion lengths for Cs diffusion on Te- and I-terminated surface areas as a function of time. As one can see in figure 6(d) the diffusion mobility of Cs on Te-terminated surface areas is very high. The room temperature diffusion length Λ of Cs adatoms reaches hundred of microns within several seconds. Therefore, according to our simulation, Cs atoms deposited on Te-terminated areas are able to reach the I-terminated surface areas through random-walk diffusion on a short time scale. The average time for an adatom to leave an area of radius R_0 can be estimated as $\langle t \rangle = \frac{1}{2\alpha} \frac{R_0^2}{D}$. If we assume the 'effective' radius of Te-terminated surface areas to be equal to the half of the characteristic length scale of the domains, i.e. ~50 nm then the average time for a Cs adatom to reach the I-terminated domain is 0.4 μs.

4. Discussion

The origin of the two-termination surface structure of BiTeI are stacking faults in the non-centrosymmetric bulk crystal [6, 7] as corroborated by our STM measurements that reveal an independence of the domain boundaries and surface step edges. The two domains form a complex mottled surface pattern with a characteristic length scale of roughly 100 nm. The domain size is therefore clearly larger than the typical length scale on which electronic quantization effects become important and thus allows for fully developed band structures parallel to the surface plane. In addition to the electronic structure also the atomic defect morphology, adsorption energies and adatom diffusion length differ for the two terminations.

We anticipate the termination domain sizes to depend on the precise crystal growth conditions [6] which might provide means to control this parameter.

The surface termination strongly influences the potential profile along the surface normal [6, 7, 12, 13]. Our results show that this potential profile is highly sensitive towards unintentionally adsorbed residual gas species which lead to considerable energy shifts in the surface band structure. The electronic structure of bare BiTeI(0001) surfaces is therefore subject to an aging effect that similarly occurs for the topological insulator surface Bi_2Se_3(0001) [32, 33]. However, in contrast to Bi_2Se_3 whose unit cell is centrosymmetric and whose surface has a homogeneous termination [29], the aging effect for BiTeI is influenced by the presence of different surface terminations. On the time scale of hours only states on I-terminated surface areas show energy changes which results from a preferential positioning of adsorbates on this termination. It is conceivable that the comparably large number of near-surface atomic defects evidenced by STM further influences the precise adsorption behaviour of the residual gas species. The observed degradation process should be taken into account, for example, in transport experiments that address the surface electronic structure of BiTeI(0001) samples, in particular if they were exposed to air. Further work will be necessary to investigate systematically the effect of different residual gas species on the electronic states.

As shown by our experiments Cs adatoms deposited on BiTeI(0001) at room temperature accumulate on I-terminated surface areas where they form islands. This self-organized segregation of adatoms on one termination type might be used to selectively dope or modify the surface electronic structure. Recently, two adjacent Te- and I-terminated domains have been proposed to realize a 'Rashba *p–n* junction' with spin-polarized carriers [35]. Selective doping of one domain type would give the opportunity to modify the potential gradient along such a junction.

5. Conclusion

We have investigated structural and electronic properties of cleaved BiTeI(0001) single crystal surfaces. Combining complementary experimental methods and DFT calculations we confirmed a coexistence of I- and Te-terminated surface domains on a length scale of 100 nm. On the atomic scale we identified characteristic defects for both terminations being located in the surface and subsurface layers. Measurements of the surface electronic structure reveal a considerable aging effect: electronic states on the I-terminated surface areas show energy changes of several 100 meV on the time scale of hours under ultra-high vacuum conditions, whereas states on the Te-terminated surface areas remain unmodified. This selective aging effect could be mimicked by room temperature deposition of Cs adatoms that are found to accumulate on I-terminated surface areas. The preferential positioning is explained by the calculated adsorption energies and diffusion length of Cs adatoms varying significantly between the two terminations.

References

[1] König M *et al* 2007 *Science* **318** 766
[2] Chen Y L *et al* 2009 *Science* **325** 178
[3] Hasan M Z *et al* 2010 *Rev. Mod. Phys.* **82** 3045–67
[4] Ishizaka K *et al* 2011 *Nat. Mater.* **10** 521
[5] Bahramy M S, Arita R and Nagaosa N 2011 *Phys. Rev.* B **84** 041202
[6] Crepaldi A *et al* 2012 *Phys. Rev. Lett.* **109** 096803
[7] Landolt G *et al* 2012 *Phys. Rev. Lett.* **109** 116403
[8] Sakano M *et al* 2012 *Phys. Rev.* B **86** 085204
[9] Landolt G *et al* 2013 *New J. Phys.* **15** 085022
[10] Sakano M *et al* 2013 *Phys. Rev. Lett.* **110** 107204
[11] Mauchain J *et al* 2013 *Phys. Rev. Lett.* **111** 126603
[12] Eremeev S V *et al* 2012 *Phys. Rev. Lett.* **108** 246802
[13] Eremeev S V, Nechaev I A and Chulkov E V 2012 *J. Exp. Theor. Phys. Lett.* **96** 437
[14] Sklyadneva I Yu *et al* 2012 *Phys. Rev.* B **86** 094302
[15] Eremeev S V, Rusinov I P, Nechaev I A and Chulkov E V 2013 *New J. Phys.* **15** 075015
[16] Zhu Z *et al* 2013 *New J. Phys.* **15** 023010
[17] Lee J S *et al* 2011 *Phys. Rev. Lett.* **107** 117401
[18] Demkó L *et al* 2012 *Phys. Rev. Lett.* **109** 167401
[19] Ogawa N *et al* 2013 *Phys. Rev.* B **88** 035130
[20] Bell C *et al* 2013 *Phys. Rev.* B **87** 081109
[21] Martin C *et al* 2013 *Phys. Rev.* B **87** 041104
[22] Wang C-R *et al* 2013 *Phys. Rev.* B **88** 081104
[23] Bahramy M S, Yang B-J, Arita R and Nagaosa N 2012 *Nat. Commun.* **3** 679
[24] Ponosov Y S *et al* 2014 *J. Exp. Theor. Phys. Lett.* **98** 557
[25] Yang B-J *et al* 2013 *Phys. Rev. Lett.* **110** 086402
[26] Xi X *et al* 2013 *Phys. Rev. Lett.* **111** 155701
[27] Tran M K *et al* 2014 *Phys. Rev. Lett.* **112** 047402
[28] Hirahara T *et al* 2011 *Phys. Rev. Lett.* **107** 166801
[29] Duarte dos Reis D *et al* 2013 *Phys. Rev.* B **88** 041404(R)
[30] Jiang Y *et al* 2012 *Phys. Rev. Lett.* **108** 066809
[31] Kong D *et al* 2011 *ACS Nano* **5** 4698
[32] Bianchi M *et al* 2011 *Phys. Rev. Lett.* **107** 086802
[33] Benia H M *et al* 2011 *Phys. Rev. Lett.* **107** 177602
[34] Seibel C *et al* 2012 *Phys. Rev.* B **86** 161105
[35] Tournier-Colletta C *et al* 2014 *Phys. Rev.* B **89** 085402
[36] Horcas I *et al* 2007 *Rev. Sci. Instrum.* **78** 013705
[37] Tomokiyo A, Okada T and Kawano S 1977 *Japan. J. Appl. Phys.* **16** 291
[38] Kokh K A, Nenashev B G, Kokh A E and Shvedenkov G Y 2005 *J. Cryst. Growth* **275** E2129
[39] Kresse G and Hafner J 1993 *Phys. Rev.* B **48** 13115
[40] Kresse G and Furthmüller J 1996 *Comput. Mater. Sci.* **6** 15

[41] Blöchl P E 1994 *Phys. Rev.* B **50** 17953

[42] Kresse G and Joubert D 1999 *Phys. Rev.* B **59** 1758

[43] Perdew J P, Burke K and Ernzerhof M 1996 *Phys. Rev. Lett.* **77** 3865

[44] Wiesendanger R 2010 *Scanning Probe Microscopy and Spectroscopy: Methods and Applications* (Cambridge: Cambridge University Press)

[45] Shevelkov A V, Dikarev E V, Shapanchenko R V and Popovkin B A 1995 *J. Solid State Chem.* **114** 379

[46] Wang C *et al* 2002 *J. Mater. Chem.* **12** 2426

[47] Gosálvez M A *et al* 2014 arXiv:1402.5920